Journal of Power Sources 192 (2009) 120–125

Contents lists available at ScienceDirect

Journal of Power Sources

journal homepage: www.elsevier.com/locate/jpowsour

Fabrication, electrochemical characterization and thermal cycling of anode supported microtubular solid oxide fuel cells

R. Campana [a,b], R.I. Merino [a,*], A. Larrea [a], I. Villarreal [b], V.M. Orera [a]

[a] Instituto de Ciencia de Materiales de Aragón, Universidad de Zaragoza-CSIC, c/Pedro Cerbuna 12, E-50009, Zaragoza, Spain
[b] IKERLAN-Energía, Parque Tecnológico de Álava, c/Juan de la Cierva 1, 01510 Miñano, Álava, Spain

ARTICLE INFO

Article history:
Received 30 September 2008
Received in revised form
22 December 2008
Accepted 23 December 2008
Available online 31 December 2008

Keywords:
Micro-SOFC
EIS
I–V
Thermal cycles

ABSTRACT

This work describes the manufacture and electrochemical characterization of anode supported microtubular SOFC's (solid oxide fuel cells). The cells consist of a Ni–YSZ anode tube of 400 μm wall-thickness and 2.4 mm inner diameter, a YSZ electrolyte of 15–20 μm thickness and a LSM–YSZ cathode. The microtubular anode supporting tubes were prepared by cold isostatic pressing. The deposition of thin layers of electrolyte and cathode are made by spray coating and dip coating respectively. The cells were electrochemically characterized with polarization curves and complex impedance measurements using 5% H_2/95% Ar and 100% of H_2, humidified at 3% as reactant gas in the anodic compartment and air in the cathodic one at temperatures between 750 and 900 °C. The complex impedance measurements show an overall resistance from 1 to 0.42 Ω cm^2 at temperatures between 750 and 900 °C with polarization of 200 mA cm^{-2}. The *I–V* measurements show maximum power densities of 0.3–0.7 W cm^{-2} in the same temperature interval, using pure H_2 humidified at 3%. Deterioration in the cathode performance for thin cathodes and high sintering temperatures was observed. They were associated to manganese losses. The cell performance did not present considerable degradation at least after 20 fast shut-down and heating thermal cycles.

1. Introduction

Solid oxide fuel cells, SOFC's, have a great potential being the cleanest, more versatile and most efficient systems for chemical to electrical energy conversion [1]. Up to now yttria-stabilized zirconia, YSZ, is the most used electrolyte material due to its good O^{2-} conductivity, excellent mechanical properties and chemical compatibility [2]. In recent years, increasing interest in microtubular SOFC's [3,4] has developed due to their higher mechanical and thermal stability, simpler seal requirements, higher power densities per unit volume and shorter times to start-up and shut-down when compared with planar and tubular conventional designs.

The cell configuration used in this study consists of a nickel and yttria-stabilized zirconia (Ni–YSZ) cermet anode supporting tube with a thin YSZ electrolyte layer and a thin lanthanum strontium manganite and yttria-stabilized zirconia (LSM–YSZ) composite cathode. The purpose of this study was to optimize the fabrication processes for these microtubular cells, focusing on the effect of cathode thickness and sintering temperature in the electrochemical performance of the cells.

Usually, in the microtubular SOFC's designs the supports are fabricated using extrusion techniques [5–7]. In our case the cells are anode supported on Ni–YSZ tubes fabricated by cold isostatic pressing. In addition the anode support geometry allows placing a thin-coated electrolyte, which reduces the electrolytic resistance losses and yields better conductance at lower temperatures than for electrolyte support set-ups [8–10].

In anode supported cells gas transport through the thick anode may contribute to polarization losses. Consequently, the tubular anode supported cell geometry requires a good permeability, low tortuousity factor for easy gas transport as well as a high number of triple-phase boundaries (TPB's), and a high mechanical and thermal stability which also implies a good adhesion with the electrolyte. In a previous work the Ni–YSZ cermet tubes were physically and electrically characterized and their microstructure optimized using half cells and platinum paste as cathode [11].

We present a complete electrochemical study of cells with different configurations measuring *I–V* curves and using EIS analysis to separate the contribution of each component to the cell. Finally, we performed degradation experiments by measuring the cell's performance, under thermal cycles, which are one of the major limitations for these systems [12].

* Corresponding author. Tel.: +34 976 761333; fax: +34 976 761229.
E-mail address: rmerino@unizar.es (R.I. Merino).

0378-7753/$ – see front matter © 2008 Elsevier B.V. All rights reserved.
doi:10.1016/j.jpowsour.2008.12.107

Table 1
Preparation conditions for the cathodes studied in the text.

Sample number	Cathode sintering temperature	Cathode thickness
1	1250 °C	100 μm
2	1250 °C	50 μm
3	1050 °C	50 μm

2. Experimental details

2.1. Cell preparation

The 10–15-cm length microtubular cells consist of a Ni–YSZ cermet anode of approximately 400 μm thickness and 2.4 mm inner diameter, an YSZ electrolyte of 15–20 μm thickness and a LSM–YSZ composite layer of thickness varying between 50 and 100 μm as cathode. Cell fabrication is made out of commercial products, NiO (Aldrich), YSZ (Tosoh) and LSM–YSZ (Fuel Cells Materials). The anodic support is Ni–YSZ 50% in volume of solid phase, with porosities around 50%. The tubular supports were fabricated according to the following steps [11]. The commercial NiO was ball milled with 2-propanol media, the binder was added to the mixture of YSZ, NiO (milled) and pore former. The samples were obtained by cold isostatic pressing at 200 MPa. The electrolyte YSZ layer was deposited by wet powder spraying (WPS) using 2-propanol as liquid vehicle. The thickness of the deposited films was controlled by weighting. Both anode and electrolyte were co-sintered at 1400 °C with 2-h dwell time. Afterwards, the cathode layers were deposited by dip coating (using 5 wt% of binder and 1% of dispersant) and sintered using two different sintering cycles either at 1250 °C with 1.5-h dwell time or at 1050 °C with 2-h dwell time. Also we varied the thicknesses of the cathode layers in order to analyse their electrochemical response. In this work, sample 1 has a 100 μm thickness cathode sintered at 1250 °C, sample 2 has a 50 μm thickness cathode sintered at 1250 °C and sample 3 has a 50 μm thickness cathode sintered at 1050 °C (Table 1). Overall, the cell preparation procedure involves simple ceramic processes, few deposition steps and just two sintering steps.

2.2. Cell characterization

The electrochemical performance of the fuel cells was tested using a four-probe set-up at temperatures between 650 and 900 °C. Different compositions, 4.85% H_2–92.15% Ar–3% H_2O and 97% H_2–3% H_2O were used as fuel, and stagnant air as the oxidant. *I–V* curves were measured between 650 and 900 °C with a home made electronic charge (Servicio de Instrumentacion Científica, Universidad de Zaragoza). Electrochemical impedance spectroscopy (EIS) measurements were performed with a VSP potentiostat with EIS capabilities from Princeton Applied Research. EIS curves were analyzed with an Ec-lab software. In the impedance spectra measurements the frequency ranges from 0.1 Hz to 500 kHz. The microstructure of the cell components was characterized after electrochemical testing by scanning electron microscopy (SEM). Energy dispersive spectroscopy (EDS) microanalysis was also done under the scanning electron microscope when needed.

The cell's degradation experiments were performed by monitoring the power density using the following cycle. The cell was heated from 20 to 900 °C in approximately 15 min. Then we measured the cell power density at 400 mA cm^{-2} for 10 min, and we cooled down the cell to 300 °C (in approximately 30 min). This procedure was repeated more than 20 times.

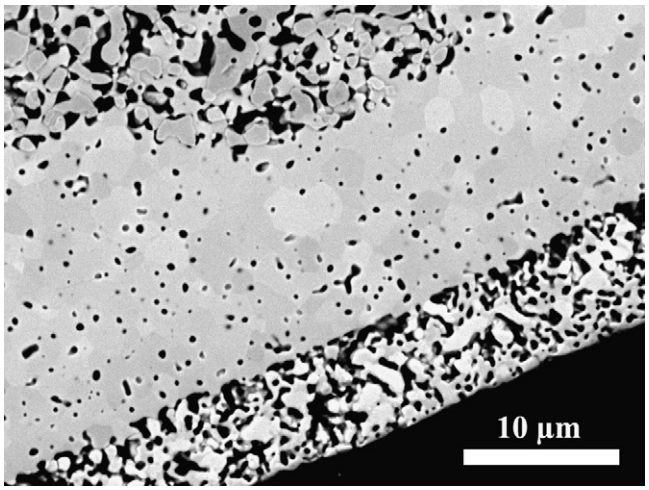

Fig. 1. Transverse cross-section SEM image of one cell, in which we can see all of the components and their interfaces: left-upper corner Ni–YSZ anode with open porosity and 400 μm thickness; middle: YSZ electrolyte with closed porosity and 20 μm thickness; down-right side: LSM–YSZ cathode with open porosity and 10 μm thickness.

3. Results and discussion

3.1. Cell preparation

In Fig. 1 we show the transverse cross-section SEM image of one cell in which we can see the microstructure of all of the cell components and their interfaces. As we can see in the micrograph, the anode has an open porosity and the size of the metallic Ni grains are close to those of the YSZ which generates a good microstructure homogeneity with a good contact between the different phases and good permeability [11]. The anode–electrolyte interface is also optimum (tree root structure). The electrolyte is tight to gas permeation.

LSM cathodes of different thickness and sintered at different temperatures were prepared. It was realized that sintering the cathodes at temperatures below 1000 °C did not result in a good electrolyte–cathode adhesion. In the cell shown in Fig. 1 the cathode layer was sintered at 1250 °C. It presents open porosity to allow the gas permeation. Also, in this picture we can appreciate the good cathode–electrolyte interface and the thickness homogeneity of the cathode layer. However, there is also a compromise between cathode thickness and sintering temperature. For 20 μm cathode layers sintered at 1250 °C, EDS microanalysis shows that about 30% of the manganese is missing, presumably because of the evaporation of manganese oxide during the sintering cycle.

Since manganese deficiency produces a decrease in the cathode electronic conductivity we conclude that well working cathodes have to be thicker than 50 μm and sintered between 1050 and 1250 °C.

3.2. I–V characterization

The *I–V* curves were measured at temperatures between 650 and 900 °C. The fuel gas flow was low, about 0.2 L min^{-1} (with 4.85% H_2), which leads to fuel utilizations close to 50% at 600 mA cm^{-2} to approach as much as possible the cell working conditions. Also we restricted the measurements to cell voltages above about 0.5 V to avoid cell deterioration.

In Fig. 2 we show the voltage and power density versus current density curves measured at 850 °C for sample 2 with 4.85% H_2–3% H_2O and 97% H_2–3% H_2O fuels respectively and stagnant air in the cathode. Using wet 4.85% H_2 mixture, the delivered power density

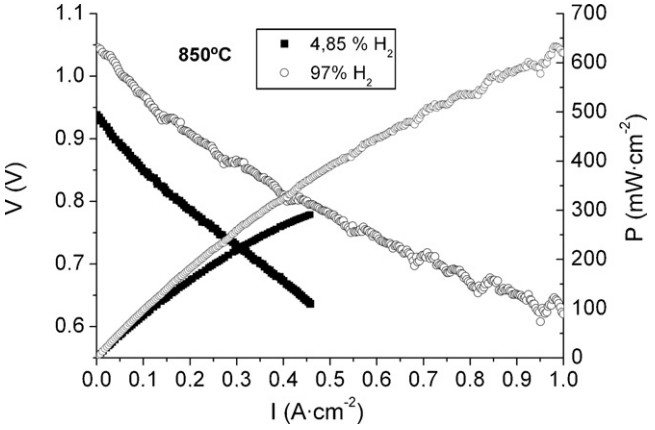

Fig. 2. *V–I* (left axis) and *P–I* (right axis) curves for sample 2, using 4.85% H_2 + 3% H_2O + 92.15 Ar and 97% H_2 + 3% H_2O.

amounts to 300 mW cm^{-2} with 0.6 V operating voltage, whereas using wet 97% H_2, the power density rises up to 650 mW cm^{-2} at the same operating voltage and temperature.

This is a consequence of the increase in the OCV (open cell voltage) Nernst potential and limiting current density (fuel availability) when the hydrogen content in the fuel increases. The experimental values for OCV are 0.94 and 1.05 V which are very close to those predicted by the Nernst equation: 0.96 and 1.08 V for 4.85% H_2–3% H_2O and 97% H_2–3% H_2O respectively. This indicates that the YSZ electrolyte films are leak- and crack-free. If we compare the slopes of the two *V–I* curves in Fig. 2 we can see that up to current densities of ≈ 400 mA cm^{-2} we have approximately the same slopes. In fact, at 350 mA cm^{-2} we have 0.57 and 0.55 Ω cm^2 for 4.85 and 97% H_2 respectively. The *V–I* slope decreases for current densities larger than 400 mA cm^{-2} with 97% of H_2. We will come back to that point later on.

According to their OCV values, the electrolytes are also leak-free in the rest of the studied cells. In Fig. 3 we give the *V–I* and *P–I* curves for the three cells studied, measured at 850 °C with the 4.85% H_2 mixture. The power density obtained for the cathode sintered at the lowest temperature (sample 3) is larger but the difference among them is less than 2%. Sample 2 shows the largest slope variation at low current densities among the samples, an indication of a larger activation polarization, most probably associated to some degradation of the thin layer of cathode during the high temperature sintering process. The trend is the same at all temperatures. The maximum power density obtained in the cells increases with temperature. For example, for sample 2 and diluted H_2 it ranges from about 0.08 W cm^{-2} at 650 °C to 0.35 W cm^{-2} at 900 °C, being the total resistances obtained from the slope of the *I–V* curves 1.7 and 0.44 Ω cm^2 respectively.

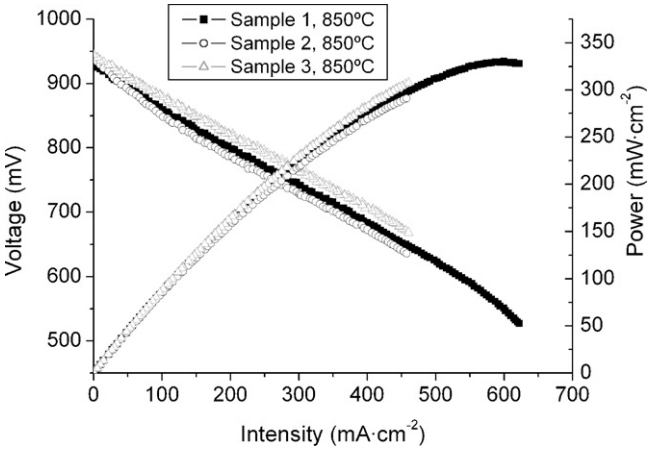

Fig. 3. *V–I* and *P–I* curves measured at 850 °C with the 4.85% H_2 wet fuel for samples 1–3.

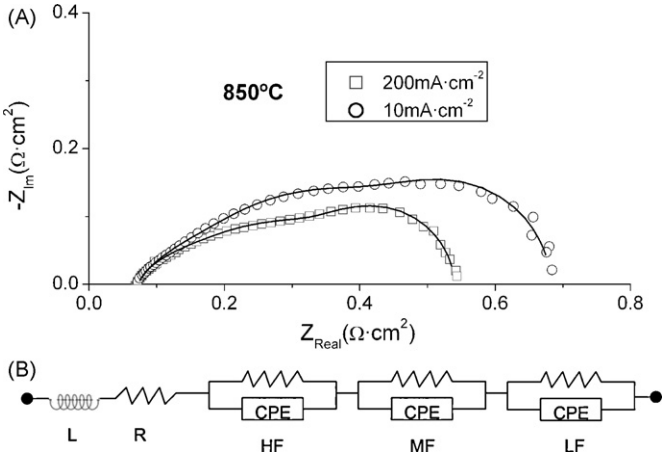

Fig. 4. (a) Nyquist diagram measured at 850 °C of sample 1 with two different polarization current densities and the corresponding fits. (b) Equivalent electrical circuit used to fit the impedance diagrams.

This *I–V* performance is competitive, together with a simple production procedure. As shown in Fig. 2, sample 2 delivers 750 mA cm^{-2} at 0.7 V and 850 °C with 97% H_2–3% H_2O and stagnant air. The diluted H_2 experiments suggest that the current density will increase by 16% on sample 1 (see Fig. 3) and thus at 0.7 V, it will deliver 870 mA cm^{-2}. Sammes et al. [13] have reported on microtubular anode supported cells 150 mA cm^{-2} at 850 °C and 0.7 V. Ding and Liu [14] anode supported cells prepared using single step sintering procedure show similar performances as ours. Other laboratories obtain similar or better performance in planar anode supported SOFC's, but using several deposition and sintering steps; up to 800 mA cm^{-2} at 0.7 V, Kim et al. [15], up to 1160 mA cm^{-2} Basu et al. [16], or 1 A cm^{-2} at 800 °C reported by Souza et al. [10].

3.3. EIS characterization

We have done complex impedance analysis of the three cells using 4.85% H_2 as fuel. In the following we will discuss the data in the 800 to 900 °C temperature range, which are the most relevant to the application. At temperatures lower than 800 °C the overall resistance increases. For example, at 750 °C this was close to 1 Ω cm^2 for all samples. In Fig. 4a we give the Nyquist diagram measured at 850 °C on sample 1 at low (10 mA cm^{-2}) and medium (200 mA cm^{-2}) bias current. The other samples present a similar behaviour.

Table 2
Overall resistances obtained from EIS measurements with different polarizations and H_2 concentrations.

Sample number	H_2 (%)	I_{pol} (mA cm^{-2})	R_{tot} (Ω cm^2) 900 °C
1	4.85	10	0.532
		200	0.427
2	4.85	10	0.791
		200	0.507
3	4.85	10	0.562
		200	0.445
2	97	0	0.816
		200	0.445
		500	0.344
		700	0.293

Table 3
Area specific resistance values ($\Omega\,cm^2$) obtained from the impedance curves using 4.85% H_2, 92.15% Ar and 3% H_2O. R_{LF} and R_{MF} values from the EIS fit, R_{ohm} has been obtained from the HF intercept of the curve with the Zreal axis. The Pol 1 and Pol 2 experiments were measured at 10 and 200 mA cm^{-2} respectively.

Sample number	T (°C)	R_{LF} anode ($\Omega\,cm^2$)		R_{MF} cathode ($\Omega\,cm^2$)		R_{ohm} ($\Omega\,cm^2$)	
		Pol 1	Pol 2	Pol 1	Pol 2	Pol 1	Pol 2
1	900	0.21	0.14	0.18	0.10	0.05	0.05
	850	0.22	0.17	0.24	0.15	0.072	0.07
	800	0.25	0.21	0.52	0.32	0.10	0.10
2	900	0.23	0.14	0.44	0.26	0.07	0.06
	850	0.25	0.13	0.60	0.31	0.08	0.08
	800	0.38	0.16	0.82	0.39	0.10	0.10
3	900	0.21	0.16	0.21	0.17	–	0.07
	850	0.22	0.15	0.21	0.21	–	0.08
	800	0.21	0.14	0.49	0.32	–	0.12

A large depressed semicircle is present at the lowest frequency (LF arc), with an inverse relaxation time ≈10 Hz. A second semicircle corresponding to a resistance of the same order of magnitude appears at intermediate frequencies (MF arc). Its inverse relaxation time depends on sample and temperature. Finally, at larger frequencies, a smaller contribution is also observed (HF arc). The pure ohmic contribution is mainly due to the electrolyte resistance. It can be obtained from the high frequency intercept of the Nyquist curve with the Zreal axis.

Table 2 shows the values of the total resistance (low frequency intercept with the Zreal axis) for the different cells measured with different concentrations of fuel and bias current densities. The total resistance of the cells clearly depends on the concentration of the fuel used and on the polarization intensity at which the measurement is carried out. It decreases as the bias current increases, in agreement with the decreasing slope of the *V–I* curves, and it decreases when we increase the concentration of the fuel, as observed in the *V–I* measurements. The results of the overall resistances obtained from EIS analysis are consistent with those from the slopes of the *I–V* curves for the different tested cells.

In order to separate the different contributions to the total resistance, we have used the equivalent electrical diagram sketched in Fig. 4b. *R* represents the pure ohmic resistance. Each of the parallel circuits of resistance and constant phase element gives account for its respective depressed semicircle from high to low frequency and from left to right in the diagram. The elements contribute from left to right to the impedance in decreasing frequency. A parasitic inductance *L* has been added to account for the measurement equipment contribution.

The low frequency (LF) arc has temperature independent, summit frequency values of 10 Hz for samples 1 and 2 and 5–6 Hz for sample 3. Its resistivity decreases by 25% when we change the bias current from 10 mA cm^{-2} to 200 mA cm^{-2}. The absence of any temperature dependence, the value of the relaxation time and the fact that we are working with anode supported SOFCs, points out towards fuel delivery and gas diffusion at the anode as the process responsible for this LF arc [2,17–19]. Moreover, its resistance is the same for all cells: 0.21, 0.23 and 0.21 $\Omega\,cm^2$ with 10 mA cm^{-2} and 0.17, 0.14 and 0.16 $\Omega\,cm^2$ with 200 mA cm^{-2} bias current for samples 1, 2 and 3 respectively, at 900 °C. If the rate limiting step is gas diffusion at the anode, as described in Ref. [20], or if it is caused by fuel consumption, the resistance can be expressed by

$$R^a_{conc} = \frac{RT}{2F}\left[\left(\frac{1}{i_{as}-i} + \frac{1}{\left((P^0_{H_2O}/P^0_{H_2})i_{as}+1\right)}\right)\right] \quad (1)$$

i_{as} is the limiting current density. From R_{LF} at 200 mA cm^{-2} bias current, we obtain limiting current densities around 800 mA cm^{-2} using the 4.85% H_2 mixture as fuel, which implies that the cells can work with reasonable current densities even with this low H_2 content fuel without fuel delivery constrains.

The medium frequency (MF) arcs present summit frequency values between 100 and 200 Hz (sample 1), 50 and 125 Hz (sample 2) and 350 and 2000 Hz (sample 3), with not a clear temperature dependence. However the frequency increases with bias current. The resistance decreases by a factor of 1.5–2 as the bias current increases from 10 to 200 mA cm^{-2}, and it is clearly temperature activated (see Table 3). The values at 900 °C and I_{bias} = 200 mA cm^{-2} are 0.10, 0.26 and 0.17 $\Omega\,cm^2$ for samples 1, 2 and 3 respectively. The values at 850 °C are similar to the LF arc resistances except for sample 2, which has higher MF resistance.

According to Jorgensen and Mogensen [21], different arcs due to LSM/YSZ composite cathodes appear in this frequency range. One whose summit frequency decreases with increasing sintering temperature (as is the case when we compare our sample 1 with sample 3), and whose magnitude increases with increasing composite thickness and is thermally activated, is associated to dissociative adsorption and transfer of species at the TPB and surface diffusion. Another one, strongly microstructure dependent and also thermally activated is attributed to transport/transfer of oxygen intermediates between LSM and YSZ. Consequently, it is quite reasonable to assume that this MF arc is due to the different processes that cause activation polarization at the cathode. For samples 1 and 3 the dependency with temperature and values of R_{MF} are quite similar and smaller than for sample 2. At 850 °C we have a decrease in factor close to 2.5–3 for the samples 1 and 3 with respect to sample 2. Then, we can conclude that the effect of lowering the cathode sintering temperature from 1250 to 1050 °C, results in a smaller contribution to the total resistance, minimizing the charge transfer and activation processes losses at the electrode. This is possibly because low sintering temperatures preserves Mn stoichiometry, ion which tends to evaporate during the cathode sintering at high temperatures. As we pointed out above, this effect is more severe in the thinner cathode films (sample 2).

The high frequency contribution to the resistivity is smaller in magnitude than the previous ones. The R_{HF} values lie about 0.07 $\Omega\,cm^2$ at 900 °C and are thermally activated. The summit frequencies, between 10^3 and 10^4 Hz, seem to increase slightly when bias current increases. However, the uncertainty in its determination by fitting of the impedance spectra is large and masks any possible difference between cells. It might be tentatively associated to activation of the anode reaction, which is generally faster than the cathode one.

Uncertainties in the resistance values obtained from the fits are small for R_{LF} in sample 3 (5–20%), which is well separated in frequency from the rest of spectra and moderate (20–50%) for R_{LF} in samples 1 and 2 where more overlap with the medium frequency arc is present. The medium frequency arcs overlap in frequency either with the low frequency arc (samples 1 and 2) or with the high

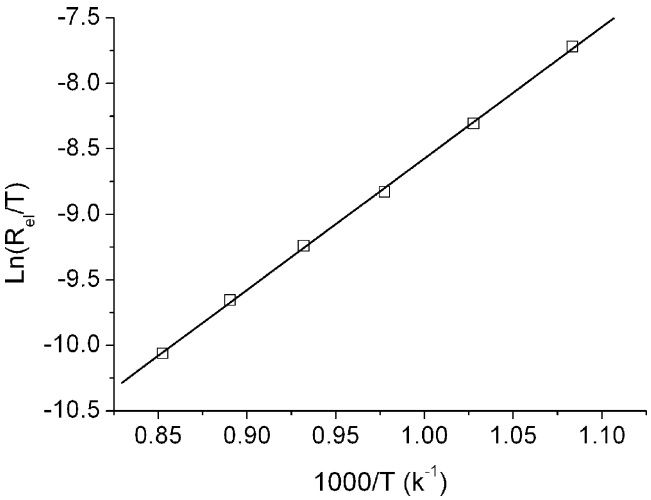

Fig. 5. $\ln(R_{ohm}/T)$ versus inverse temperature. R is measured in $\Omega\,cm^2$ and T in K. The line is the fit to the exponential law.

frequency arc (sample 3) and consequently the resistance values are determined from the fits with moderate to large uncertainties (20–70%). In spite of this, the trends observed for R_{LF} and R_{MF} in the temperature interval 800–900 °C are clear and distinctive, as explained in the previous paragraphs and we can be reasonably confident of the relative magnitude of both dominating processes to the polarization. At lower temperatures, the observed trends in the resistance values that result from the fits are not so clear. For example, a temperature dependence seems to appear on R_{LF}. This is probably a result of different dominating processes contributing to the polarization in the lowest temperature range that we did not try to disclose.

Finally, from the high frequency intercept with the Zreal axis, the ohmic contribution has been determined (R_{ohm}, also given in Table 3 for the measurements showing such intercept). For solid oxide fuel cells, the ohmic contribution to the polarization $\eta_{ohm} = R_{ohm} i$ at a given current density is given by

$$\eta_{ohm} = (\rho_e l_e + \rho_a l_a + \rho_c l_c + R_{contact})\, i \quad (2)$$

where ρ is the cell component resistivities and l their thickness.

In Fig. 5, we show as an example, the dependence of the $\ln(R_{ohm}/T)$, with the inverse temperature for sample 1. As can be seen, the fitting to the exponential law is excellent, and gives an activation energy of 0.86 eV, the expected one for the YSZ electrolyte. This value is in good agreement with Ref. [16] (0.90 eV) and with our own experiments on an 8YSZ pellet (0.92 eV in the same temperature range). An indication that the main contribution to R_{ohm} is due to the electrolyte.

3.4. Thermal cycles

Finally, several thermal and current load cycles have been performed in order to study the cell stability. In Fig. 6a we present the thermal cycles used in this experiment which corresponds to the faster heating and cooling steps we can achieve with our furnace. In Fig. 6b we present the variation of the cell power output at 400 mA cm^{-2} along 20 thermal cycles. At each cycle we plot the voltage recorded every second along 10 min. One can see in the figure that the cell electrochemical performance is not reduced at all during the thermal cycles. We must note that we have not done yet redox experiments but we expect a strong resistance to redox cycles because our sample tubes that are reduced in the central zone and remains oxidized close to the open ends can be tested and thermally cycled safely.

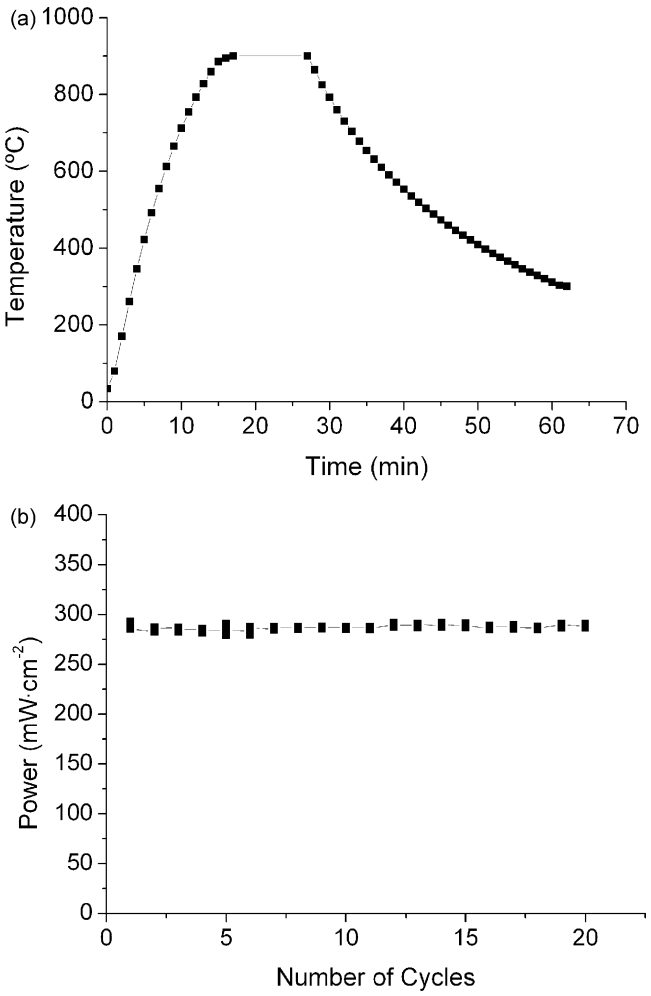

Fig. 6. (a) The thermal cycle used in the thermal shock experiments. (b) Cell power output along 20 sudden thermal cycles. After each thermal cycle we plot the voltage measured every second along 10 min waiting time.

4. Summary

Optimization of anode performance and electrolyte and cathode integration allows fabricating in a reproducible way, efficient mini-tubular Ni–YSZ/YSZ/LSM cells using cheap technologies. The cells show an operation total area specific resistance of 0.5 $\Omega\,cm^2$ and maximum power densities of up to 0.33 W cm^{-2} at 850 °C using safe H_2 as fuel, and more than 0.6 W cm^{-2} using 97% H_2–3% H_2O. Using EIS techniques and an equivalent circuit model, we could separate the different contributions of the cell components to polarization losses. The most important conclusion is that attention has to be paid to cathode fabrication to avoid Mn losses. Manganese evaporation is more noticeable when cathode thickness is small and sintering temperatures are high. Also, we tested the cells under thermal shock conditions and the cell's electrochemical performance is not reduced after more than 20 severe thermal cycles.

Acknowledgements

The results were obtained under projects financed by the Spanish Government and the European Community (FEDER program): MAT2006-13005 C03-01 and CIT-120000-2007-50. We thank Dr. J. Gurauskis for helping us with rheological measurements.

References

[1] N.Q. Minh, J. Am. Ceram. Soc. 76 (3) (1993) 563–588.
[2] S.C. Singhal, K. Kendal, High Temperature Solid Oxide Fuel Cells: Fundamental, Design and Applications, Elsevier, Oxford, 2003.
[3] N.M. Sammes, R.J. Boersma, G.A. Tompsett, Solid State Ionics 135 (2000) 487–491.
[4] G.A. Tompsett, C. Finnerty, K. Kendall, T. Alston, N.M. Sammes, J. Power Sources 86 (2000) 376–382.
[5] Y. Du, N.M. Sammes, G.A. Tompsett, J. Eur. Ceram. Soc. 20 (2000) 959–965.
[6] Y. Du, N.M. Sammes, J. Eur. Ceram. Soc. 21 (2001) 727–735.
[7] I.P. Kilbride, J. Power Sources 61 (1996) 167–171.
[8] K. Chen, Z. Lü, N. Ai, X. Huang, Y. Zhang, X. Ge, X. Xin, X. Chen, W. Su, Solid State Ionics 177 (2007) 3455–3460.
[9] J. Will, A. Mitterdorfer, C. Kleinlogel, D. Perednis, L.J. Gauckler, Solid State Ionics 131 (2000) 79–96.
[10] S. de Souza, S.J. Visco, L.D. De Jonghe, J. Electrochem. Soc. 144 (1977) L35–L37.
[11] R. Campana, A. Larrea, R.I. Merino, I. Villarreal, V.M. Orera, Bol. Soc. Esp. Ceram. V. 47 (2008) 189–195.
[12] W. Bujalski, C.M. Dikwal, K. Kendall, J. Power Sources 171 (2007) 96–100.
[13] N.M. Sammes, Y. Du, R. Bove, J. Power Sources 145 (2005) 428–434.
[14] J. Ding, J. Liu, J. Am. Ceram. Soc. 91 (10) (2008) 3303–3307.
[15] S.D. Kim, S.H. Hyun, J. Moon, J.-H. Kim, R.H. Song, J. Power Sources 139 (2005) 67–72.
[16] R.N. Basu, G. Blass, H.P. Buchkremer, D. Stöver, F. Tietz, E. Wessel, I.C. Vinke, J. Am. Ceram. Soc. 25 (2005) 463–471.
[17] M. Lang, C. Auer, A. Eismann, P. Szabo, N. Wagner, Electrochim. Acta 53 (2008) 7509–7513.
[18] Q.A. Huang, R. Hui, B. Wang, J. Zhang, Electrochim. Acta 52 (2007) 8144–8164.
[19] N. Wagner, W. Schurnberger, B. Müller, M. Lang, Electrochim. Acta 43 (1998) 3785–3793.
[20] J.W. Kim, A.V. Virkar, K.Z. Fung, K. Mehta, S.C. Singhal, J. Electrochem. Soc. 146 (1) (1999) 69–78.
[21] M.J. Jorgensen, M. Mogensen, J. Electrochem. Soc. 148 (2001) A433–442.